LETTER

Novel rubidium lead chloride nanocrystals: synthesis and characterization

To cite this article: Daniel Amgar *et al* 2017 *Nano Futures* **1** 021002

View the article online for updates and enhancements.

Related content

- Solution-phase synthesis of rubidium lead iodide orthorhombic perovskite nanowires
  Da-Hye Lim, Parthiban Ramasamy, Do-Hyun Kwak et al.

- Room-temperature synthesis of ultra-small, near-unity single-sized lead halide perovskite quantum dots with wide color emission tunability, high color purity and high brightness
  Lucheng Peng, Jing Geng, Lisha Ai et al.

- Size-tunable near-infrared PbS nanoparticles synthesized from lead carboxylate and sulfurwith oleylamine as stabilizer
  Jincheng Liu, Huangzhong Yu, Zhonglian Wu et al.

NANO FUTURES

Novel rubidium lead chloride nanocrystals: synthesis and characterization

Daniel Amgar[1], **Małgorzata Wierzbowska**[2], **Vladimir Uvarov**[1], **Vitaly Gutkin**[1] and **Lioz Etgar**[1]

[1] The Institute of Chemistry, The Center for Nanoscience and Nanotechnology, The Casali Center for Applied Chemistry, The Hebrew University of Jerusalem, Jerusalem, Israel
[2] Institute of High Pressure Physics, Polish Academy of Sciences, Sokołowska 29/37, 01-142 Warsaw, Poland

E-mail: lioz.etgar@mail.huji.ac.il

Abstract

Alkali ternary lead halides have been studied intensively in the past few years, with great interest focussed on perovskite materials. In this paper we report on novel rubidium lead chloride nanocrystals (NCs) with the formula $Rb_6Pb_5Cl_{16}$, which adopt a tetragonal symmetry. The NCs were characterized and found to be active in the UV region, with a band-gap of ~4.05 eV. The roles of the ligands, oleic acid and oleylamine, were investigated and found to strongly affect the morphology and composition of the NCs, through the stabilization of the facilitated crystallization of the ionic precursors. The effective masses were observed by density functional theory (DFT) calculations, using the dielectric function, and the the Bohr exciton radius and exciton binding energy of the NCs were estimated. Moreover, the results were supported by the DFT calculations of the electronic properties and atomic structure.

Introduction

Recently, knowledge about ternary lead (Pb) halides has increased rapidly with evolving research about perovskite compounds. Organic–inorganic and fully-inorganic perovskite materials have been studied intensively in the last few years, mostly in the optoelectronic and solar fields. The excellent properties of perovskites as light harvesting materials in the visible spectrum showed great applicative potential, both in bulk and nanometric forms. Particularly, the enthusiasm around the fully-inorganic perovskite derived, at first, from stability issues. Eperon *et al* reported that replacing the common organic methylammonium (MA) cation with the inorganic cesium (Cs) cation highly improves the thermal stability of the perovskite, which is a decisive factor in solar cells activity [1]. The major studies of nanometric fully-inorganic perovskite dealt with Cs-based perovskite. Protesescue *et al* reported on fully-inorganic nanocrystals (NCs) with intriguing optical properties, bright and sharp emissions, high photoluminescence quantum yields (PLQY), and high absorption coefficients [2]. Few studies have reported on tuning the composition of the perovskite by replacing certain atoms in the perovskite formula AMX_3 (A-monovalent cation, M-divalent metal cation, X-halide) in order to discover new features and improvements, including mixed-cation systems [3–6]. One of the possible A-cation candidates that was suggested to replace the MA cation [3, 7] was the rubidium (Rb) cation, for its advantage as an oxidation-stable mono-valent cation. The formability of Rb-based perovskite can be calculated by the tolerance factor equation $t = \frac{(r_A + r_X)}{[\sqrt{2}(r_M + r_X)]}$, which determines whether a compound will form a perovskite structure or not [8]. Based on the tolerance factor, it was claimed that Rb^+, which is only slightly smaller than Cs^+, is too small in order to fit in the cuboctahedral cage of the A-cation in the bulk perovskite structure [3, 9], according to the perovskite expected formability range $0.81 < t < 1.01$ [10, 11]. The tolerance factors of $RbPbCl_3$, $RbPbBr_3$, and $RbPbI_3$ are 0.785, 0.781, and 0.776, respectively. Apparently, the rubidium (Rb) cation does not fit in the perovskite bulk structure, but on the other hand, the synthesis of nanometric Rb-based perovskite has never

been published. The surface chemistry of nanocrystals differs from bulk due to a looser structure, thus it is conceivable that perovskite formation would occur in the nanoscale in different conditions than bulk. For instance, $CsPbI_3$ was investigated as a light harvesting bulk material in solar cells and found to be very problematic for its unstable cubic black phase and high annealing temperature [1]. However, the synthesis of $CsPbI_3$ NCs is simple in that cubic $CsPbI_3$ perovskite NCs are obtained at lower temperatures [2]. Likewise, it is very intriguing to learn how the replacement of the A-cation will affect the properties of the perovskite crystal, optics, and activity in the nanometric sizes. Ghanbari and co-workers reported on $RbPbI_3$ nanostructures for photocatalysis, synthesized by the hydrothermal method, and investigated how different molar ratios of $RbI:PbI_2$, reaction time and temperature affect the size and shape of the product [12]. Moreover, $RbPbI_3$ nanowires were reported. The $RbPbI_3$ nanowires were found to absorb below 450 nm and exhibited a good photoresponsive activity, suggesting a potential in the optoelectronic field [13]. According to literature, integrating Rb in the perovskite lattice results in structural distortions that can lead to a different perovskite or non-perovskite phase [14, 15]. Beck *et al* reported for the first time and investigated the synthesis and crystal structure of $Rb_6Pb_5Cl_{16}$ phase [16]. $Rb_6Pb_5Cl_{16}$ was found to crystallize in the tetragonal space group $P4/mbm$ with a variety of different coordination polyhedra for the cations. Later, Monzel *et al* [17] reported on redetermination of the phase diagram $RbCl/PbCl_2$, which was first reported in [9]. They stated that $RbPbCl_3$ is unstable at room temperature and can be stabilized only above 320 °C. The reinvestigation also revealed the existence of the $Rb_6Pb_5Cl_{16}$ phase, which is stable at room temperature. Furthermore, Linaburg reported on perovskite phases of $RbPbCl_3$, $RbPbBr_3$, and $RbPbI_3$ adopting a cubic symmetry at elevated temperatures, while in room temperature a mixture of tetragonal $Rb_6Pb_5Cl_{16}$ and monoclinic $RbPb_2C_5$ phases is obtained [9]. This reinforces the possibility to fabricate rubidum lead halide crystals. It is important to develop more perovskite and perovskite-like compositions and structures in order to expand their variety of applications. As mentioned above, $RbPbCl_3$ has the highest tolerance factor, which encouraged us to perform a synthesis of rubidium lead halide NCs.

Herein, we report on the synthesis of novel rubidium lead chloride NCs with the formula $Rb_6Pb_5Cl_{16}$. This is the first report on NCs of this material, also using rubidium carbonate (Rb_2CO_3) as a new precursor for obtaining this compound, other than RbCl [3, 9]. Physical, structural, and optical characterizations are shown and discussed. To support the experimental results, we performed theoretical calculations, using density functional theory (DFT) method [18], to determine the effective masses, dielectric constant, and the Bohr radius of the NCs.
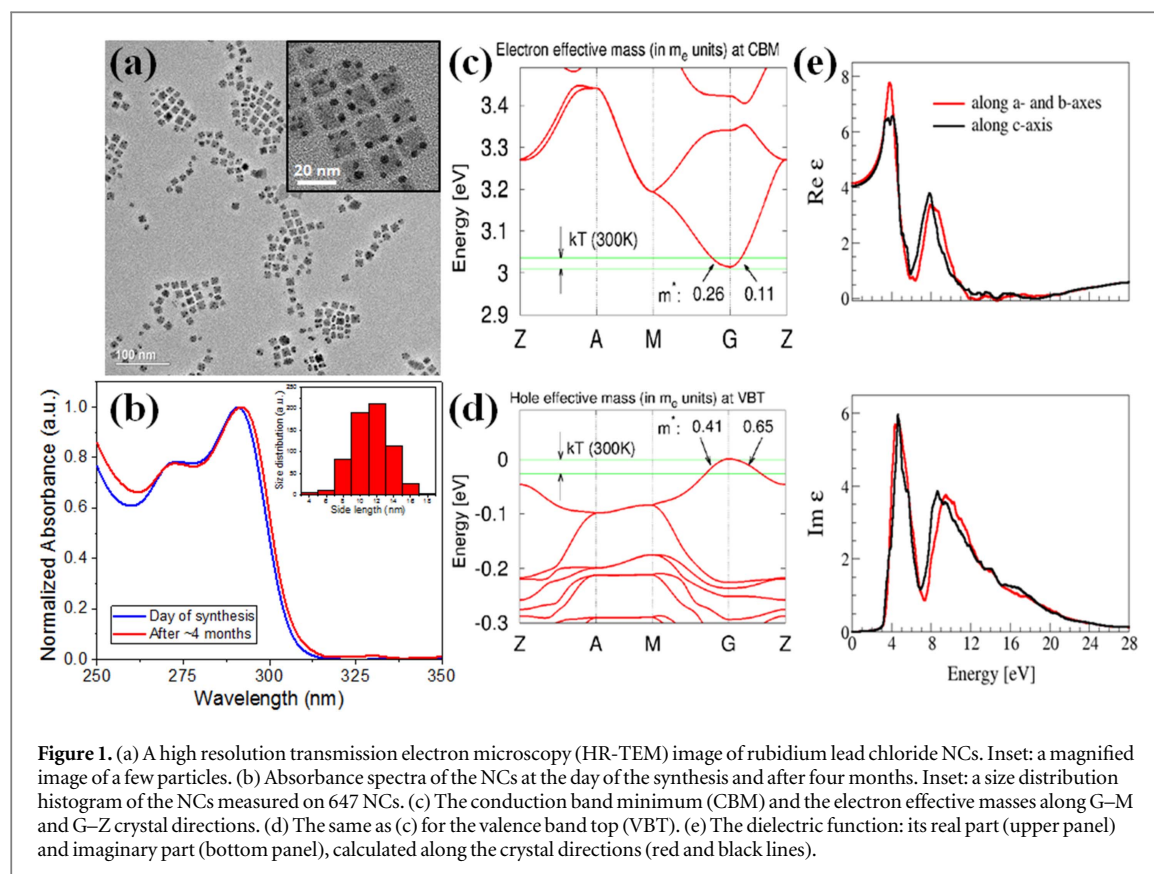
Results and discussion

Rubidium lead halide NCs were synthesized by a hot injection method according to the published procedure of Protesescue *et al* [2, 19]. Briefly, two precursor solutions were prepared. The first solution contained Rb_2CO_3, oleic acid (OA), and 1-octadecene (ODE), the second solution contained lead chloride ($PbCl_2$), OA, oleylamine (OLA), tri-n-octylphosphine (TOP), and ODE, while OA and OLA were in a volume ratio of 1:1. Both flasks were heated to 120 °C for 1 h under vacuum conditions for degassing. Afterwards, the temperature was raised to 150 °C in both flasks under argon flow. A desired volume of Rb-oleate precursor was injected into the $PbCl_2$ precursor solution and the reaction was quenched with an ice bath after a few seconds. The product was precipitated twice with isopropanol to give a white precipitate and re-dispersed with hexane for further characterizations.

Figure 1(a) shows high resolution transmission electron microscope (HR-TEM) images of the as-synthesized NCs with a square-like shape. The inset of figure 1(a) presents a magnified image of the NCs, revealing some clear black spots upon the NCs (discussed below in further detail).

Figure 1(b) presents the absorbance spectra of the NCs measured at the day of the synthesis and after ~4 months while stored in ambient conditions. The absorbance peaks remained unchanged, showing the long-term stability of these NCs. The absorbance peak is located at ~291 nm and the onset is at ~306 nm, which corresponds to a band-gap of ~4.05 eV. Therefore, the optical activity of the obtained NCs is in the UV spectral region. The band gap of the bulk crystal is 3.01 eV obtained with DFT calculations and 4.13 eV with the pseudopotential self-interaction correction (pSIC) method [20]. This is in good agreement with the absorption measurement (see figure S1 is available online at stacks.iop.org/NANOF/1/021002/mmedia in the supporting information (SI)). The inset in figure 1(b) shows a size distribution histogram, based on more than 600 NCs, showing the average side length of the NCs to be 11.29 $\pm$ 0.04 nm (the size distribution histogram was calculated from data obtained using ImageJ software). In this particles analysis there was an assumption of square-shaped NCs.

The band-structure derived effective masses, averaged over the crystal directions at the valence band top (VBT) and conduction band minimum (CBM), which are 0.53 and 0.19 of the electron mass (m_e) for holes and

Figure 1. (a) A high resolution transmission electron microscopy (HR-TEM) image of rubidium lead chloride NCs. Inset: a magnified image of a few particles. (b) Absorbance spectra of the NCs at the day of the synthesis and after four months. Inset: a size distribution histogram of the NCs measured on 647 NCs. (c) The conduction band minimum (CBM) and the electron effective masses along G–M and G–Z crystal directions. (d) The same as (c) for the valence band top (VBT). (e) The dielectric function: its real part (upper panel) and imaginary part (bottom panel), calculated along the crystal directions (red and black lines).

electrons, respectively (see figures 1(c), (d)). These numbers, together with the calculated dielectric function and its static value $\varepsilon(0)/\varepsilon^{vacc} = 4.1$ (figure 1(e)), led to the exciton Bohr radius $a_0 = 1.584$ nm and the exciton binding energy $E_b = 0.111$ eV. There is a close resemblance between the obtained parameters for $Rb_6Pb_5Cl_{16}$ and the corresponding numbers for cesium lead halide ($CsPbX_3$) compounds [2].

Furthermore, the crystal structure of the NCs was investigated via structural analysis. X-ray diffraction (XRD) measurements were preformed and the results are presented in figure 2(a). The XRD pattern corresponds to a $Rb_6Pb_5Cl_{16}$ tetragonal phase, which is a non-perovskite phase. This phase was discovered by Monzel *et al* [17] during their work on redetermination of the phase diagram RbCl/PbCl$_2$, as mentioned earlier. An important insight of this work was that the perovskite phase RbPbCl$_3$ cannot exist at room temperature, but as a mixture of the two previously unknown phases, $Rb_6Pb_5Cl_{16}$ and $RbPb_2Cl_5$; only with the application of heat a phase transition can occur to get the perovskite phase. The first phase transition occurs above 320° to a tetragonal phase of RbPbCl$_3$. Higher temperatures resulted in the cubic phase of RbPbCl$_3$ perovskite. A repeating XRD measurement of the NCs detected 9.8% of Pb_2O_3 phase inside the $Rb_6Pb_5Cl_{16}$ NCs and 90.2% of $Rb_6Pb_5Cl_{16}$ phase (see figure S2 in the SI). The Pb_2O_3 phase can be assigned to the black spots in the $Rb_6Pb_5Cl_{16}$ NCs shown in figure 1(a). Previous work on $CsPbX_3$ NCs reported on black spots that appear as a response to the electron beam during the TEM analysis [21]. In this case, the black spots were integrated in the NCs and were observed in 'fresh' areas of the TEM grid, with minimal exposure to the beam. Nonetheless, the black spots became clearer and larger with longer exposure to the electron beam along with decomposition of the brighter parts. There is an obvious difference in the contrasts of the grey nanocrystals and the black spots on top of them (figure 1(a)); this can be implied for high concentrations of Pb, which has a higher electron density than the other atoms in this compound, resulting in a higher contrast.

Dark scanning transmission electron microscopy (STEM) and energy-dispersive x-ray spectroscopy (EDS) were applied in order to confirm the composition of the NCs and the black spots inside the NCs, as can been seen in figures 2(b) and S3. In figure S3, the EDS spectrum detected the atoms Rb, Pb, Cl and O in the region of interest. The quantification analysis that followed determined the atomic percentage of the atoms to be 17.40, 28.89, 37.62, and 16.07, respectively. The reasonable assumption is that the ratio between Rb and Pb is ~1:1, according to the XRD, so that the remaining Pb atoms were possibly bound to the detected O atoms to create a Pb oxide phase or alternatively, metallic Pb nanoparticles, as previously reported for similar observations [22].

The inset of figure 2(b) shows an HR-TEM image of a black spot (within the NC) with the corresponding fast Fourier transform (FFT), related to plane (111) of metallic Pb. More areas were scanned and the results are presented in the SI section (figure S4). EDS analysis (figure S3) indicated a higher content of Pb, reinforcing the
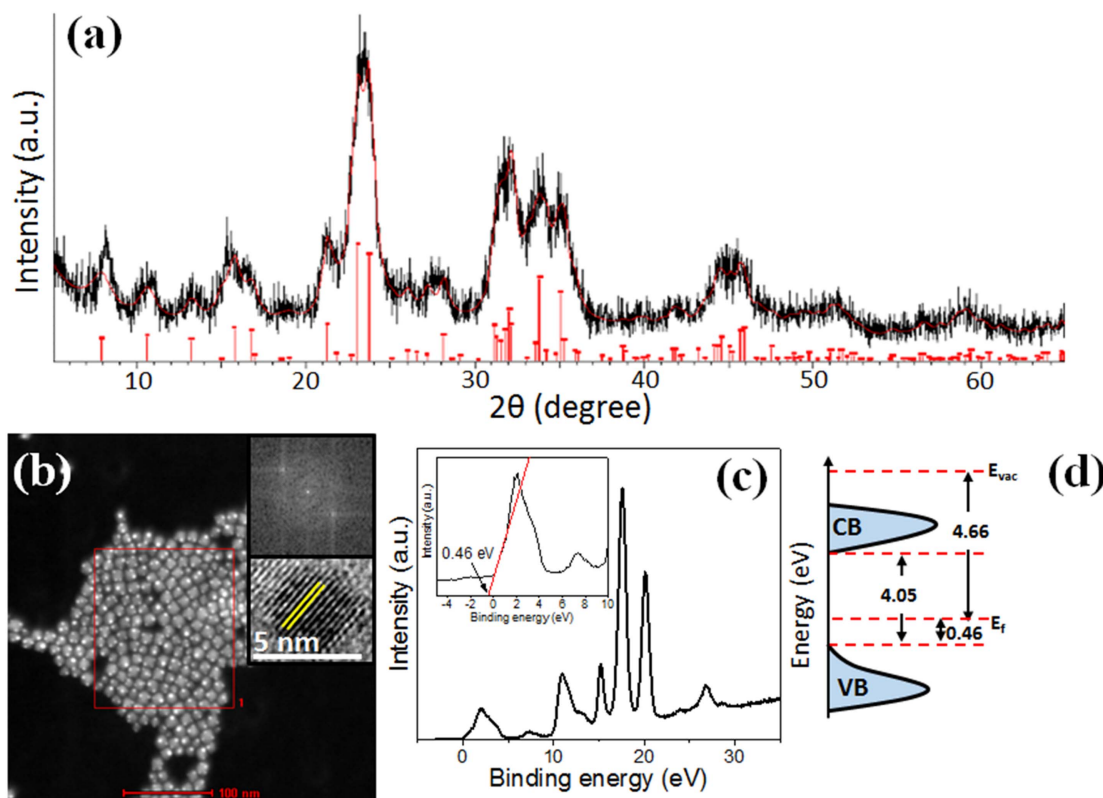
Figure 2. (a) Experimental (black) and simulated (red) x-ray diffraction (XRD) patterns of rubidium lead chloride NCs that show the correspondance to a tetragonal $Rb_6Pb_5Cl_{16}$ phase. (b) A scanning transmission electron microscopy (STEM) image. Insets: high magnification of a Pb-rich particle inside a $Rb_6Pb_5Cl_{16}$ NC with d-spacing that corresponds to plane (111) of metallic Pb and its corresponding FFT. (c) X-ray photoelectron spectroscopy (XPS) spectrum of the NCs measuring electronic states in the valence band. Inset: a magnified area of the graph near the valence band edge. (d) A schematic overview of the band diagram of the NCs.

assumption of the black Pb-rich particles within the $Rb_6Pb_5Cl_{16}$ NCs to be either Pb oxide or metallic Pb nanoparticles. It is predicted that the Pb-terminated surface opens the octahedral hole with Rb^+ in the center, which is a sensitive adsorption site for the O atoms from the OA; leading to a termination of its molecules with the H–C=O group, instead of COOH. This scenario is consistent with the crystallographic data which reports 9.8% of Pb_2O_3 phase in the reported NCs (figure S2). The Rb atom takes a role of a cation in the crystal, thus its properties to bind O are opposite to the electron-rich elements of the VI-group (i.e. Se)—present for example in PbSe where the Pb_xO_y-type structures are not found [23].

X-ray photoelectron spectroscopy (XPS) analysis (figure S5) detected the presence of Rb, Pb, and Cl atoms with a ratio of ∼1:1 between Rb and Pb, as expected. The atomic percentage of Cl was lower than expected, as described in table S1 in the SI section. This may have occured due to evaporation of Cl_2 molecules during the measurement.

In order to study the electronic properties of these $Rb_6Pb_5Cl_{16}$ NCs more deeply, valence band (VB) XPS measurement and surface photovoltage spectroscopy (SPV) were performed. The valence band XPS measurement was applied for determination of the valence band (figure 2(c)). This measurement gives information about the density and occupancy of electronic states in the valence band of the material, while the edge of the graph gives an evaluation of the VBT. The inset of figure 2(c) presents the extracted VB value, 0.46 eV below the Fermi level. The work function of the NCs was measured using the SPV method and found to be 4.63 eV. An overview of the band diagram of the NCs is presented in figure 2(d).

To learn more about the influence of the ligands on the features and crystallization process of the $Rb_6Pb_5Cl_{16}$ NCs, a study of the ligands' roles was conducted. As described earlier, the ligand ratio in the $PbCl_2$ precursor solution was 1:1. Keeping the total molar content of both ligands constant, mixtures of OA:OLA in a volume ratios of 1:2 and 1:3 were synthesized and studied. The use of an OA and OLA pair is well-known in the syntheses of perovskite NCs [24]. There is a dynamic equilibrium of acid/base in similar colloidal systems [25]. In this case, the OA donates a proton to the OLA and turns into an oleate anion, as the OLA ligand is protonated and turns into an oleylamminium cation [26]. Figure 3(a) depicts an HR-TEM image of 1:2 OA:OLA NCs in which few morphologies are observed, including relatively large rectangles, long thin nanowires (NWs) consisting of small black dots, and distorted square-like phase, similar to the NCs with a 1:1 ratio (figure 1(a)). Upon increasing the
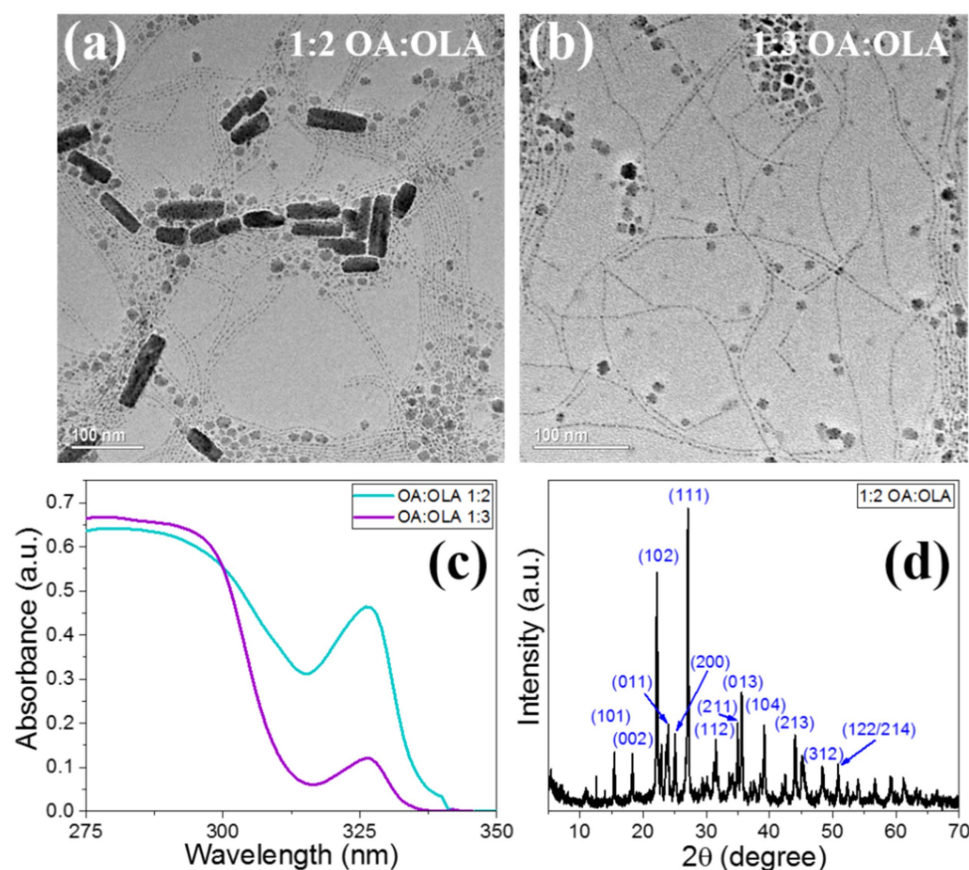
Figure 3. HR-TEM images of obtained NCs with volume ratio of 1:2 (a) and 1:3 (b) of oleic acid (OA) and oleylamine (OLA), respectively (OA:OLA). (c) Absorbance spectra of the NCs in both cases. (d) An XRD pattern of the NCs with 1:2 ratio of OA:OLA that corresponds to a main orthorhombic phase of Pb(OH)Cl. The spectrum of the NCs with ligands ratio 1:3 OA:OLA is similar to the one presented in (d) and can be found in the SI section, figure S6.

OLA concentration to 1:3 OA:OLA, as shown in the HR-TEM image in figure 3(b), there were similar observations to that of the 1:2 OA:OLA NCs; in this case, the large rectangles do not appear. A synthesis with OLA alone (without OA) was carried out as well for a complete investigation, however, a minimal volume of OA is necessary in order to completely dissolve the $PbCl_2$. Therefore, the OA has an important role in solubilizing the $PbCl_2$ [2]. Based on the HR-TEM images, it seems that an increase of OLA excess in this synthesis affects the NCs' shape. It was previously claimed that acid–base pair has a definite impact on the morphology and optical properties of a similar system of perovskite NCs [25]. The new morphologies can be an indication that the binding of OLA to the surface is chemical and not physical, so variable amounts of OLA ligands can change the growth directions of the NCs by blocking certain crystallographic facets. However, if the concentration of OLA is increased at the expense of the OA, it may reduce the protonation process, resulting in fewer protonated OLA species, i.e., fewer oleylammonium cations. These conditions may increase the coordinative bonding of the unprotonated OLA species with the Pb^{2+} cations on the surface, rather than the electrostatic interaction of the oleylammonium cations with the Cl^- anions in the lattice. This can explain the elongated structures that appear in figures 3(a) and (b). The absorbance measurement is shown in figure 3(c) presenting an optical red shift, relative to the OA:OLA 1:1 case, with peak position at ~326 nm and onset at ~336 nm. The unexpected optical shift can indicate a possible change in the chemical composition. To decipher these results, XRD measurement was applied for the 1:2 product. Surprisingly, the XRD spectrum detected a main orthorhombic Pb(OH)Cl phase (figure 3(d)). The XRD peaks perfectly matched the standard XRD pattern of orthorhombic Pb(OH)Cl. Previously, few works reported on the mineral Pb(OH)Cl [27–30]; Chen *et al* reported on Pb(OH)Cl nanotubes that absorb in the UV region, at 258 nm and 292 nm [27], which is similar to the absorbance of the obtained nanostructures. A possible explanation for the phase transfer into Pb(OH)Cl, based on both TEM and XRD analyses, is that higher content of unprotonated OLA ligands may interact with larger areas on the surface of the NCs and avoid Rb-oleate species from participating in the crystallization of the NCs, yielding in another Rb-free crystal phase of Pb(OH)Cl. In addition to the Pb(OH)Cl phase, the XRD of the 1:2 product also detected minor content of Pb_2O_3 and $Rb_6Pb_5Cl_{16}$ phases. In comparison, the XRD of the 1:3 product detected only the Pb(OH)Cl phase (figure S6). This strengthens the suggested mechanism that an increase of OLA content enhances the
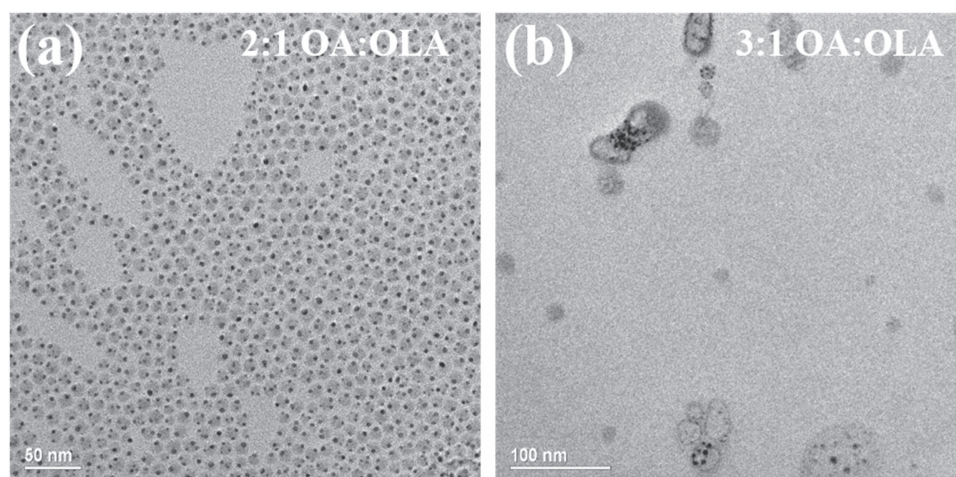
Figure 4. HR-TEM images of rubidium lead chloride NCs with volume ratios of (a) 2:1 and (b) 3:1 of oleic acid (OA) and oleylamine (OLA) ligands.

formation of Pb(OH)Cl, repelling Rb-oleate species in the growth processes. For a better insight into this issue, the interaction of the Pb-terminated (001) surface with the OA molecules was simulated. A shorter molecule than the OA molecule was used for the simulation (see figure S7), since the COOH group is the functional group, which attached to the NCs surface. Three plausible geometric configurations were assumed (figure S8) and their atomic structures were optimized. Two of these reactions end up with the O atom on top of Rb from a cavity of the triangular shape set by three Pb surface atoms. The formation energy is -2.88 eV in a case when the acid molecule swaps the $-$OH termination into $=$O and $-$H, attached directly to the C atom which lost $=$O (see figure S7). The $-$OH group can also build the surface; if it takes the position between two Pb atoms, then the formation energy is -2.59 eV (see figure S8). Before the reaction, no charge transfer was observed to the surface, thus the band structure was not affected by proximity with the acid (see figure S9). In contrast, the adsorption of O or OH affects the band gap, as expected (see band structures in figure S10). Both cases cause the red shift; it is about 0.4 eV for the oxygen adsorption case, and it seems to be a multi-excitation between many impurity states for the surface reaction with $-$OH. However, the oscillator strengths need to be further investigated with more advanced methods, in order to find which optical transitions are active.

In addition, the opposite case was examined to further understand the ligands' roles. Accordingly, syntheses with ligand ratios of 2:1 OA:OLA and 3:1 OA:OLA (figures 4(a) and (b)) were performed. In figure 4(a), the obtained NCs have a distorted shape, compared to the 1:1 OA:OLA NCs. According to literature, the oleate ligands are effective in the control of the size of more isotropic structures [25], as seen in figure 4(a), and in contrast to the case of OLA excess. In the case of 3:1 OA:OLA ratio, as presented in figure 4(b), the NCs did not form at all. The reason for that can be an insufficient amount of OLA which can severely affect the stabilization of the forming NCs. The concentration of OLA is probably too small to form free-standing NCs due to less coordinative bonding of oleylammonium ligands to the metal cations on the surface.

Conclusions

This paper reports the synthesis of rubidium lead chloride NCs as a novel UV-active material with intriguing features and a complicated structure. HR-TEM analysis revealed some speckled square-like shaped NCs and XRD determined the symmetry of the tetragonal $Rb_6Pb_5Cl_{16}$ phase. Theoretical calculations of electronic and structural properties were correlated with the experimental data. Different ligand ratios appeared to change the morphology and crystal structure of the NCs into a main phase of Pb(OH)Cl with an optical red shift. The suggested mechanism indicates that a high content of OLA relative to OA can affect the crystallization process by insufficient oleylammonium species to stabilize the Pb cations. In this case there is more coordinative bonding of unprotonated OLA ligands to the Pb cations on the surface, which minimizes the interaction of Rb-oleate species with the growing surface. The result indicates a main Pb(OH)Cl phase without any Rb cations in the lattice. Work by Shu *et al* [28] suggests that Pb(OH)Cl material can function as an anode for lithium-ion battaries, which can be very attractive in the nanometric scale as well. Moreover, it can function as a precursor in the synthesis of PbSe nanocrystals [30].

Future experiments will focus on synthesis modifications in order to achieve the perovskite phase of RbPbCl$_3$ in the nanoscale, as well as in the bulk form. The UV optical properties of the as-synthesized NCs can be utilized for ultra violet light emitting diodes (UV-LED) or lasing applications.

Experimental

Chemicals
Rubidium carbonate (Rb$_2$CO$_3$, 99%, Sigma-Aldrich), lead (II) chloride (PbCl$_2$, 98%, Sigma-Aldrich), OA (90%, Sigma-Aldrich), OLA (70%, Sigma-Aldrich), ODE (90%, Sigma-Aldrich), trioctylphosphine (TOP, 97%, Strem), 2-propanol ($\geqslant$99.8%, Sigma-Aldrich), and hexane (not pure, Gadot) were purchased and used as received, without any further purification.

Preparation of Rb-oleate
Rb-oleate precursor was prepared according to the previous published procedure by Protesescue *et al* [2]: 0.138 g of Rb$_2$CO$_3$ was mixed with 625 μl of OA and 7.5 ml of ODE in a 100 ml three-neck flask. The solution was degassed for 1 h under vacuum at 120 °C and then heated to 150 °C under argon flow.

Synthesis of Rb$_6$Pb$_5$Cl$_{16}$ NCs
The NCs were synthesized according to Protesescue *et al* [2]: 0.052 g of PbCl$_2$ was mixed with 0.5 ml of OA, 0.5 ml of OLA, 1 ml of TOP, and 5 ml of ODE in an additional 100 ml three-neck flask. The mixture was degassed for 1 h under vacuum at 120 °C and then heated to 150 °C under argon flow. The reaction was carried out by injection of 0.4 ml of the Rb-oleate precursor solution into the PbCl$_2$ precursor solution. The reaction was quenched using an ice bath after a few seconds. Isopropanol was added to the crude solution in a volume ratio of 1:1 and the NCs were centrifuged at 6000 rpm for 10 min. The last stage was repeated once and then the purified NCs were dispersed in hexane for further characterization.

Transmission electron microscopy (TEM)
Morphology and elemental composition of NCs were analyzed with a high resolution scanning transmission electron microscope (HR (S)TEM) Tecnai F20 G2 (FEI Company, USA). Sample preparation was performed as follows: 3.5 μl of the NCs dispersion was dropped on a copper grid coated with amorphous carbon film, then the solvent was evaporated using a vacuum chamber. Elemental analysis of NCs was done with an energy dispersive x-ray spectroscopy (EDAX EDS) when the microscope was operated in STEM mode at an accelerating voltage of 200 kV.

X-ray diffraction (XRD)
Powder x-ray diffraction measurements were performed on the D8 Advance Diffractometer (Bruker AXS, Karlsruhe, Germany) with a secondary graphite monochromator, 2° Soller slits, and a 0.2 mm receiving slit. The powder samples were placed on low background quartz sample holders. XRD patterns were within the range 3 °C–65 °C. 2θ were recorded at room temperature using CuKα radiation (λ = 1.5418 Å) with the following measurement conditions: tube voltage of 40 kV, tube current of 40 mA, step-scan mode with a step size of 0.02° 2θ, and counting time of 1 s per step.

Absorption measurements
Absorption spectra were recorded using a Jasco V- 670 spectrophotometer.

X-ray photoelectron spectroscopy (XPS)
The electronic structure and chemical state of the Rb$_6$Pb$_5$Cl$_{16}$ NCs were characterized by the XPS. The XPS measurements were done using a Kratos Axis Ultra x-ray photoelectron spectrometer (Karatos Analytical Ltd, Manchester, UK). Spectra were acquired using an Al Kα monochromatic radiation source (1486.7 eV) with 90° take-off angle (normal to analyzer). The vacuum pressure in the analyzing chamber was maintained at 2 $\times$ 10^{-9} Torr. The XPS spectra were collected with pass energy 20 eV and step 0.1 eV. The binding energies were calibrated relative to the C 1s peak energy position at 285.0 eV. Data analyses were done using a Casa XPS (Casa Software Ltd) and the Vision data processing program (Kratos Analytical Ltd).

Surface photovoltage spectroscopy (SPS)
Work function (*WF*) measurement was performed using the SKP5050-SPS040 system. The contact potential difference (*CPD*) between the sample and the vibrating tip was measured by the Kelvin probe technique. The sample was measured in a Faraday cage under air environment at three different points. Before the

measurement, the sample was stabilized with a tip for about 15 min. The scan direction was from long to short wavelength. The *WF* was calculated according to: $WF_{sample} = WF_{tip} + CPD$. The *WF* function of the tip was calibrated above the gold stage.

Density functional theory (DFT)

The pseudopotential based plane-wave code, named Quantum ESPRESSO [31], was used for the DFT calculations. We have our pSIC implementation [32] in the above package. The band structures were accurately interpolated via the matrix elements of the Hamiltonian between the maximally-localized Wannier functions [33] obtained with the Wannier90 code [34]. The formation energies were calculated from the total energies of the substrates and the final atomic configuration, via the formula: $E_{form} = E_{total}$ (surface + adsorbate)$–E_{total}$ (surface)$–E_{total}$ (adsorbate). The hole and electron effective masses were estimated from the densely interpolated bands at the VBT and CBM, respectively, via the equation $\frac{1}{m*} = \frac{1}{\hbar^2}\frac{\partial^2 E(k)}{\partial k^2}$. The dielectric function was calculated with the epsilon.x code from the Quantum ESPRESSO suite. Thus, the excitonic parameters were obtained from the relations: $a_0 = \frac{4\pi\hbar^2\varepsilon\varepsilon^{vacc}}{m*e^2}$ and $E_b = \frac{m*}{m_e\varepsilon^2}13.61$ eV. Further details are given in SI [35].

Competing financial interests

The authors decelare no competing financial interests.

Acknowledgments

References

[1] Eperon G E, Paterno G M, Sutton R J, Zampetti A, Haghighirad A A, Cacialli F and Snaith H J 2015 Inorganic caesium lead iodide perovskite solar cells *J. Mater. Chem.* A **3** 19688

[2] Protesescue L, Yakunin S, Bodnarchuk M I, Krieg F, Caputo R, Hendon C H, Yang R X, Walsh A and Kovalenko M V 2015 Nanocrystals of cesium lead halide perovskites ($CsPbX_3$, X=Cl, Br, and I): novel optoelectronic materials showing bright emission with wide color gamut *Nano Lett.* **15** 3692

[3] Saliba M *et al* 2016 Incorporation of rubidium cations into perovskite solar cells improves photovoltaic performance *Science* **354** 206

[4] Nie Z *et al* 2016 Layered and Pb-Free organic–inorganic perovskite materials for ultraviolet photoresponse: (010)-oriented $(CH_3NH_3)_2MnCl_4$ thin film *ACS Appl. Mater. Interfaces* **8** 28187

[5] Marshall K P, Walker M, Walton R I and Hatton R A 2016 Enhanced stability and efficiency in hole-transport-layer-free $CsSnI_3$ perovskite photovoltaics *Nat. Energy* **1** 16178

[6] Hao F, Stoumpos C C, Cao D H, Chang R P H and Kanatzidis M G 2014 Lead-free solid-state organic–inorganic halide perovskite solar cells *Nat. Photon.* **8** 489

[7] Trots D M and Myagkota S V 2008 High-temperature structural evolution of caesium and rubidium triiodoplumbates *J. Phys. Chem. Solids* **69** 2520

[8] Goldschmidt V M and der Krystallochemie D G 1926 *Naturwissenschaften* **14** 477

[9] Linaburg M R 2015 Studies of Halide Perovskites $CsPbX_3$, $RbPbX_3$ (X=Cl$^-$, Br$^-$, I$^-$), and Their Solid Solutions *MSc Thesis* The Ohio State University

[10] Kieslich G, Sun S J and Cheetham A K 2014 Solid-state principles applied to organic–inorganic perovskites: new tricks for an old dog *Chem. Sci.* **5** 4712

[11] Filip M R, Eperon G E, Snaith H J and Giustino F 2014 Steric engineering of metal-halide perovskites with tunable optical band gaps *Nat. Commun.* **5** 5757

[12] Ghanbari M, Sabet M and Salavati-Niasari M 2016 Synthesis and characterization of different morophologies of $RbPbI_3$ nanostructures via simple hydrothermal method and investigation of their photocatalytic activity *J. Mater. Sci., Mater. Electron.* **27** 8826

[13] Lim D-H, Ramasamy P, Kwak D-H and Lee J-S 2017 Solution-phase synthesis of rubidium lead iodide orthorhombic perovskite nanowires *Nanotechnology* **28** 255601

[14] Howard C J and Stokes H T 1998 Group-theoretical analysis of octahedral tilting in perovskites *Acta Cryst.* **54** 782

[15] Glazer A M 1972 The classification of tilted octahedra in perovskites *Acta Crys.* **28** 3384

[16] Beck H P, Schramm M and Haberkorn R 1998 Synthesis and crystal structure of $Rb_6Pb_5Cl_{16}$ *Z. Anorg. Allg. Chem.* **624** 393

[17] Monzel H, Schramm M, Towe K and Beck H P 2000 Zur Neuuntersuchung des Phasendiagramms $RbCl/PbCl_2$ *Z. Anorg. Allg. Chem.* **626** 408

[18] Kohn W and Sham L J 1965 Self-consistent equations including exchange and correlation effects *Phys. Rev.* **140** 1133

[19] de Mello Donega C, Liljeroth P and Vanmaekelbergh D 2005 Physicochemical evaluation of the hot-injection method, a synthesis route for monodisperse nanocrystals *Small* **12** 1152

[20] Filippetti A and Spaldin N A 2003 Self-interaction-corrected pseudopotential scheme for magnetic and strongly-correlated systems *Phys. Rev.* B **67** 125109

[21] Akkerman Q A *et al* 2016 Solution synthesis approach to colloidal cesium lead halide perovskite nanoplatelets with monolayer-level thickness control *J. Am. Chem. Soc.* **138** 1010

[22] Sichert J A *et al* 2015 Quantum size effect in organometal halide perovskite nanoplatelets *Nano Lett.* **15** 6521

Letters

[23] Ma W, Swisher S L, Ewers T, Engel J, Ferry V E, Atwater H A and Alivisatos A P 2011 Photovoltaic performance of ultrasmall PbSe quantum dots *ACS Nano* **5** 8140

[24] Boles M A, Ling D, Hyeon T and Talapin D V 2016 The surface science of nanocrystals *Nat. Mater.* **15** 141

[25] Pan A, He B, Fan X, Liu Z, Urban J J, Alivisatos A P, He L and Liu Y 2016 Insight into the ligand-mediated synthesis of colloidal CsPbBr$_3$ perovskite nanocrystals: the role of organic acid, base, and cesium *ACS Nano* **10** 7943

[26] De Roo J, Ibanez M, Geiregat P, Nedelcu G, Walravens W, Maes J, Martins J C, Van Driessche I, Kovalenko M V and Hens Z 2016 Highly dynamic ligand binding and light absorption coefficient of cesium lead bromide perovskite nanocrystals *ACS Nano* **10** 2071

[27] Chen Y, Wu Q-S, Yin R-H and Ding Y-P 2007 Facile fabrication and optical properties of novel Pb(OH)Cl nanotubes *J. Nanopart. Res.* **9** 283

[28] Shu J, Ma R, Shao L, Shui M, Wang D, Wu K, Long N and Ren Y 2013 Hydrothermal fabrication of lead hydroxide chloride as a novel anode material for lithium-ion batteries *Electrochim. Acta* **102** 381

[29] Woensdregt C F and Hartman P 1988 Structural morphology of cotunnite, PbCl$_2$, laurionite, Pb(OH)Cl, and SbSI *J. Cryst. Growth* **87** 561

[30] Shen H, Li J, Shang H, Niu J, Xu W, Wang H, Guo F and Li L S 2013 Phosphine-free synthesis from 1D Pb(OH)Cl nanowires to 0D and 1D PbSe nanocrystals *ACS Appl. Mater. Interfaces* **5** 10331

[31] Giannozzi P *et al* 2009 Quantum espresso: a modular and open-source software project for quantum simulations of materials *J. Phys. Condens. Matter* **21** 395502

[32] Wierzbowska M and Majewski J A 2011 Forces and atomic relaxation in density functional theory with the pseudopotential self-interaction correction *Phys. Rev. B* **84** 245129

[33] Marzari N, Mostofi A A, Yates J R, Souza I and Vanderbilt D 2012 Maximally localized wannier functions: theory and applications *Rev. Mod. Phys.* **84** 1419

[34] Mostofi A A, Yates Y R, Lee Y S, Souza I, Vanderbilt D and Marzari N 2008 Wannier90: a tool for obtaining maximally-localised Wannier functions *Comput. Phys. Commun.* **178** 685

[35] http://nextnano.com/nextnano3/tutorial/1Dtutorial_QW_exciton.htm